Design and Analysis of a Self-Orienting Wireless Power Transfer System for the Multifunctional Capsule Robot

Wei Wang, Jinlei Jiang, Weicheng Wang, Xinyuan Cui, Guozheng Yan, and Daxiang Cui

***Abstract*—Existing wireless power transfer (WPT) systems for the multifunctional capsule robot (MCR) exhibit significant fluctuations in received power, which greatly diminish the reliability of the robotic system. This article presents a self-orienting wireless power transfer (SOWPT) system based on coupled magnetic fields. A novel gyroscope-inspired power receiving device (PRD) is designed to maintain the one-dimensional receiving coil inside the PRD axial alignment with the one-dimensional transmitting coil, thereby enabling omnidirectional power transfer for the MCR. The theoretical model of power transfer for the SOWPT system is developed through theoretical analysis and finite element analysis. A finite-element model for human electromagnetic exposure safety is developed, and the electromagnetic safety compliance of the SOWPT is validated. Finally, a prototype of the SOWPT system has been fabricated. An experimental testbed is constructed to evaluate the received power on the load. Experimental results demonstrate that under emulated practical conditions, the normalized standard deviation and the maximum-to-minimum ratio of the received power on the load are 13.86% and 163.41%, respectively. These values are substantially lower than those of conventional WPT systems, validating the enhanced robustness of the proposed SOWPT system. A temperature rise experiment is performed on the PRD, validating its operational safety under designated working conditions. Furthermore, the developed theoretical model of power transfer is experimentally verified, laying the theoretical foundation for subsequent optimization.**

***Index Terms*—Capsule robot, coupled magnetic field, gyroscope-inspired, self-orienting, wireless power transfer (WPT).**

Received 19 June 2025; revised 1 October 2025; accepted 16 November 2025. Date of publication 21 November 2025; date of current version 25 February 2026. This work was supported in part by the National Natural Science Foundation of China under Grant 82020108017 and Grant 81921002, in part by the Shanghai Science and Technology Commission under Grant 21DZ2203200 and Grant 20142201300, in part by the National Facility for Translational Medicine (Shanghai) Open Project Fund under Grant TMSK-2021-302, and in part by the China Postdoctoral Science Foundation under Grant 2023M732267. Recommended for publication by Associate Editor B. Lee. *(Wei Wang and Jinlei Jiang contributed equally to this work.) (Corresponding author: Daxiang Cui.)*

Wei Wang, Jinlei Jiang, Weicheng Wang, and Daxiang Cui are with the School of Automation and Intelligent Sensing, Shanghai Jiao Tong University, Shanghai 200240, China (e-mail: aries-wang@sjtu.edu.cn; sjtujjl@sjtu.edu.cn; wangweichenghong@sjtu.edu.cn; dxcui@sjtu.edu.cn).

Guozheng Yan is with the School of Biomedical Engineering, Shanghai Jiao Tong University, Shanghai 200240, China (e-mail: gzhyan@sjtu.edu.cn).

Xinyuan Cui is with the School of Medicine, Shanghai Jiao Tong University, Shanghai 200025, China (e-mail: cuixinyuan@sjtu.edu.cn).

Color versions of one or more figures in this article are available at https://doi.org/10.1109/TPEL.2025.3635774.

Digital Object Identifier 10.1109/TPEL.2025.3635774

NOMENCLATURE

Acronyms

WPT	Wireless power transfer.
MCR	Multifunctional capsule robot.
SOWPT	Self-orienting wireless power transfer.
PRD	Power receiving device.
RC	Receiving coil.
1DRC	One-dimensional receiving coil.
3DRC	Three-dimensional receiving coil.
TC	Transmitting coil.
1DTC	One-dimensional transmitting coil.
3DTC	Three-dimensional transmitting coil.
NSD	Normalized standard deviation.
MMR	Maximum-to-minimum ratio.
EPM	External permanent magnet.
IPM	Internal permanent magnet.
SAR	Specific energy absorption rate.

Symbols and variables

V_t, I_t, C_t, L_t, and R_t	Driving voltage, driving current, tuning capacitance, self-inductance, and equivalent series resistance at the transmitting end, respectively.
I_r, C_r, L_r, R_r, and R_L	Current, tuning capacitance, self-inductance, equivalent series resistance, and load at the receiving end, respectively.
P_L	Received power on the load.
M	Mutual inductance coefficient between the TC and the RC.
μ_0	Permeability of vacuum, $\mu_0 = 4\times10^{-7}$ H/m.
μ_r	Relative permeability of the medium.
N	Number of turns of the TC.
r_t	Radius of the TC.
d	Center-to-center distance of adjacent EPMs.
$\mathbf{B_{SC}}$, $\mathbf{B_{HC}}$	Magnetic flux density of the single coil and the Helmholtz coil, respectively.
$\boldsymbol{B_P}$	Magnetic flux density generated by the total current loop at any point Q

	(x, y, z) outside the permanent magnet.
$\mathbf{B_{PA}}$	Magnetic flux density of the static magnetic field of the EPM array.
B_e	Effective magnetic flux density of the SOWPT system.
P_{Li}	Measurement values of the P_L.
σ_{PL}, λ_{PL}	NSD and MMR of the P_{Li}, respectively.
T, ΔT	Temperature and temperature rise of the PRD, respectively.

I. Introduction

GASTROINTESTINAL disorders have become increasingly prevalent worldwide, posing significant threats to human health and mortality [1]. The conventional electronic endoscope, due to its elongated tubular structure, often causes patient discomfort and complications during examinations. Additionally, this structural design limits its ability to reach deep into most parts of the small intestine, thereby reducing its effectiveness for accurate diagnosis. To address these limitations, capsule endoscopy has been developed [2]. The capsule endoscope, which is pill-sized, is ingested orally by the patient to perform examinations within the gastrointestinal tract [3], [4]. However, due to its passive locomotion and limited diagnostic capabilities, among other factors, it exhibits relatively high false-negative and false-positive rates. Consequently, it currently serves only as a complementary device to conventional electronic endoscopes. Currently, the MCR equipped with capabilities such as active locomotion [5], [6], [7], multimodal imaging [8], [9], [10], biopsy [11], [12], [13], and therapeutic functions [14], [15], [16] have become a major research focus for the next generation of gastrointestinal diagnostic technologies. However, traditional button batteries cannot meet the power requirements of the MCR, which is integrated with diagnostic and therapeutic functions. Based on electromagnetic induction coupling, WPT technology holds promise to solve the power supply challenge for the MCR.

Earlier research by some scholars focused on the WPT system employing a 1DTC paired with a 1DRC [17], [18], [19]. The advantage of this traditional 1DTC-1DRC configuration lies in the relatively simple structure of both the transmitting and receiving ends. However, this configuration induces significant fluctuations in the effective projected area of the RC relative to the TC. This results in precarious received power, including instances where it drops to zero. Consequently, the WPT system capable of providing an omnidirectional and stable power supply to MCR has garnered significant research attention. The WPT system, employing a 1DTC paired with a 3DRC, has been studied most extensively. For the design of the 3DRC, some researchers [20], [21] have developed three orthogonal coils wound around ferrite cubic cores. To minimize the overall length of the MCR, Meng et al. [22] and Jia et al. [23] designed a hollow cylindrical 3DRC mounted onto the robot body. The three orthogonal coils are stacked on top of each other, which will significantly reduce the received power of the coil located in the inner layer. Additionally, due to this overlapping structure, the received power will dramatically vary with changes in the *RC* attitude. Theoretically, the MMR of the received power reaches 300%. In actual working conditions, this ratio is even larger, which will significantly reduce the stability and reliability of the MCR system. Therefore, some researchers [24], [25], [26], [27], [28] have studied using 1DRC and changing the direction of the magnetic field generated by TC in real time to achieve a stable power supply. Zhang et al. [24], Wen et al. [25], and Han et al. [26] employ the 3DTC-1DRC configuration. The operational principle of this WPT system involves real-time monitoring of the RC's attitude through integrated sensors, followed by dynamic adjustment of the current amplitude and phase applied to the TC. This closed-loop regulation enables continuous alignment between the resultant magnetic field vector and the central axis of the RC. However, there is a significant mutual inductance among the three individual coils of the 3DTC, making it difficult to control the direction of the resultant magnetic field accurately. To address the mutual inductance of the coils, Gao et al. [27] and Zhuang, et al. [28] proposed rotating a one or two-dimensional TC via motor actuation to alter the orientation of the resultant magnetic field. This scheme can eliminate or reduce the influence of mutual inductance, but further research is needed to determine whether the rotating drive device of the TC can quickly respond to the attitude changes of the RC.

To address these issues, this article proposes a novel SOWPT system that couples alternating magnetic fields with static magnetic fields.

The rest of this article is organized as follows. In Section II, an SOWPT system comprising external and internal modules is designed, and an equivalent circuit model of the system is established. In Section III, based on combined theoretical analysis and finite element analysis, a theoretical model of power transfer integrating the alternating magnetic field and the static magnetic field is established. A finite-element model for human electromagnetic exposure safety is developed. In Section IV, a prototype of the system is fabricated, and the received power on the load is tested under simulated actual working conditions. And temperature rise experiment is performed on the PRD. In Section V, the overall performance of this system is discussed by combining theoretical models with experimental results. Finally, Section VI concludes this article.

II. Design of the SOWPT System

A. Structure of the SOWPT System

The overall structural schematic diagram of the SOWPT system is shown in Fig. 1, which comprises an external module and an internal module. The external module includes a transmitting circuit, a TC, and an external permanent magnet (EPM) array. The TC utilizes a one-dimensional Helmholtz coil. The transmitting circuit supplies the TC with alternating current at the required frequency, which drives the TC to generate an alternating magnetic field of the corresponding frequency in the working region. The internal module consists of a PRD and a receiving circuit. The RC inside the PRD induces the alternating magnetic field, thereby generating an alternating voltage. The

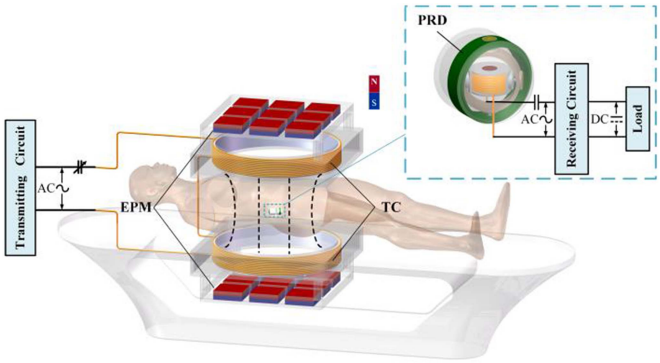

Fig. 1. Overall structure of the SOWPT system.

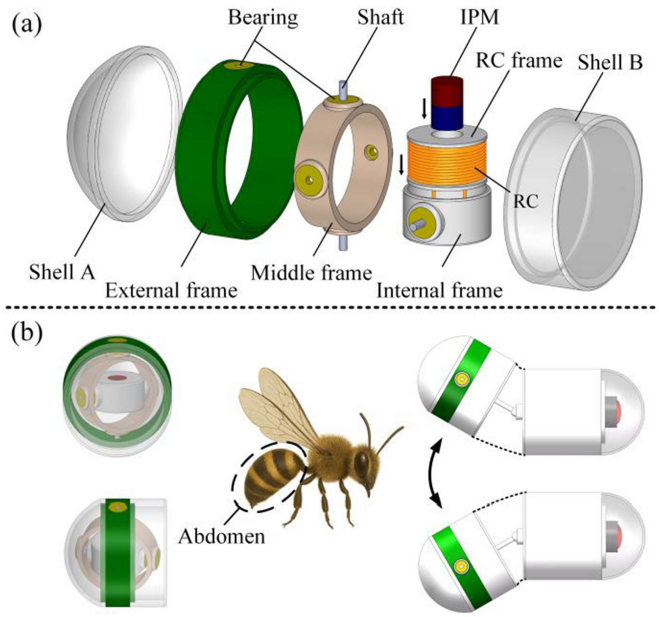

Fig. 2. Schematic diagram of (a) exploded view of the PRD structure and (b) the spherical joint between the PRD and MCR.

alternating voltage is then rectified and regulated by the receiving circuit to supply power to the MCR.

Inspired by the gyroscope, a PRD capable of achieving two degrees of freedom in rotation has been designed, as illustrated in Fig. 2(a). The PRD is composed of shell A, shell B, bearings, shaft, external frame, middle frame, internal frame, RC, RC frame, and internal permanent magnet (IPM).

The RC utilizes a one-dimensional coil. The internal frame, RC, RC frame, and IPM constitute the RC rotor. The RC rotor achieves two degrees of freedom in rotation through the gyroscopic structure. The IPM maintains the axial alignment of the RC with the TC under the influence of the static magnetic field generated by the EPM array. Based on imitating the body structure of insects such as bees, the PRD is connected to the MCR body through a ball joint, as shown in Fig. 2(b).

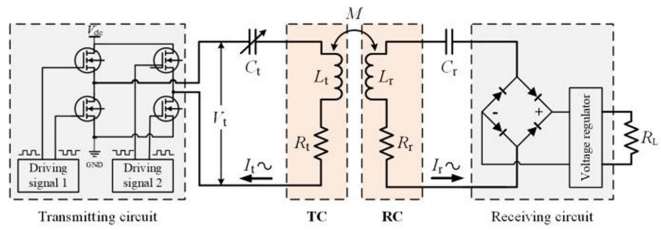

Fig. 3. Equivalent circuit of the SOWPT system.

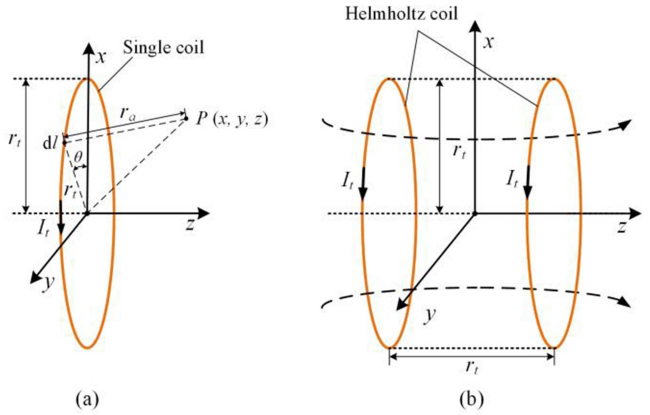

Fig. 4. Alternating magnetic field theoretical analysis of the (a) single coil, and (b) Helmholtz coil.

B. Equivalent Circuit Model of the SOWPT System

The equivalent circuit of the SOWPT system is illustrated in Fig. 3. In this figure, V_t, I_t, C_t, L_t, and R_t represent the driving voltage, driving current, tuning capacitance, self-inductance, and equivalent series resistance at the transmitting end, respectively. I_r, C_r, L_r, R_r, and R_L denote the current, tuning capacitance, self-inductance, equivalent series resistance, and load at the receiving end, respectively. M is the mutual inductance coefficient between the TC and the RC. The equivalent circuit loop equation can be expressed as

$$\begin{bmatrix} V_t \\ 0 \end{bmatrix} = \begin{bmatrix} R_t + j\omega L_t + \frac{1}{j\omega C_t} & -j\omega M \\ -j\omega M & R_r + j\omega L_r + \frac{1}{j\omega C_r} + R_L \end{bmatrix} \times \begin{bmatrix} I_t \\ I_r \end{bmatrix} \tag{1}$$

where $\omega = 2\pi f$ is the angular frequency of the driving voltage, and f is the frequency of the driving voltage.

By adjusting C_t and C_r, the transmitting and receiving circuits are tuned to resonance, respectively. According to previous research [9], when both the transmitting and receiving circuits are resonant, the received power on the load P_L can be calculated as

$$P_L = {I_r}^2 \cdot R_L = \frac{4\pi^2 f^2 M^2 I_t^2}{(R_r + R_L)^2} \cdot R_L. \tag{2}$$

III. Magnetic Field Analysis of the SOWPT System

The proposed SOWPT system comprises two types of magnetic fields: one is the alternating magnetic field generated by the TC, and the other is the static magnetic field produced by the EPM array. The alternating magnetic field is employed for power transfer, and the static magnetic field is used to maintain the axial alignment of the RC with the TC. Theoretical modeling and finite element analysis are conducted for both types of magnetic fields.

A. Alternating Magnetic Field Analysis

Taking a single coil as the analysis subject, a spatial Cartesian coordinate system is established with the center of the coil as the origin, as shown in Fig. 4(a). Based on the Biot–Savart law, the expression for the magnetic flux density $\boldsymbol{B_{SC}}$ at any point P (x, y, z) in space can be denoted as

$$\begin{cases} \boldsymbol{B_{SC}}(x,y,z) = B_{SC-x}\boldsymbol{i} + B_{SC-y}\boldsymbol{j} + B_{SC-z}\boldsymbol{k} \\ B_{SC-x} = \frac{\mu_0 N I_t r_t}{4\pi} \cdot \int_0^{2\pi} \frac{z\cos\theta}{{r_a}^3} d\theta \\ B_{SC-y} = \frac{\mu_0 N I_t r_t}{4\pi} \cdot \int_0^{2\pi} \frac{z\sin\theta}{{r_a}^3} d\theta \\ B_{SC-z} = \frac{\mu_0 N I_t r_t}{4\pi} \cdot \int_0^{2\pi} \frac{r_t - x\cos\theta - y\cos\theta}{{r_a}^3} d\theta \\ r_a = \sqrt{x^2+y^2+z^2+{r_t}^2-2x\cdot r_t\cos\theta - 2y\cdot r_t\sin\theta} \end{cases} \tag{3}$$

where $B_{SC\text{-}x}$, $B_{SC\text{-}y}$, and $B_{SC\text{-}z}$ are the components of $\boldsymbol{B_{SC}}$ along the x, y, and z axes, respectively. $\boldsymbol{i}$, $\boldsymbol{j}$, and $\boldsymbol{k}$ are the unit vectors in the directions of the x, y, and z axes, respectively. μ_0 is the permeability of vacuum, $\mu_0 = 4 \times 10^{-7}$ H/m. N is the number of turns of the coil, r_t is the radius of the TC, r_a is the distance from point P to the current element dl, and θ is the angle between the current element dl and the positive x-direction.

Due to the excellent magnetic field uniformity, the proposed SOWPT system utilizes a Helmholtz coil as the TC, which consists of two identical circular coils with a center-to-center separation equal to the coil radius. A Cartesian coordinate system is established with the origin located at the center of the dual coils, as shown in Fig. 4(b). Based on (3), the magnetic flux density $\boldsymbol{B_{HC}}$ of the Helmholtz coil can be derived as follows:

$$\begin{cases} \boldsymbol{B_{HC}}(x,y,z) = B_{HC-x}\boldsymbol{i} + B_{HC-y}\boldsymbol{j} + B_{HC-z}\boldsymbol{k} \\ B_{HC-x} = B_{SC-x}(x,y,\frac{r_t}{2}) + B_{SC-x}(x,y,-\frac{r_t}{2}) \\ B_{HC-y} = B_{SC-y}(x,y,\frac{r_t}{2}) + B_{SC-y}(x,y,-\frac{r_t}{2}) \\ B_{HC-z} = B_{SC-z}(x,y,\frac{r_t}{2}) + B_{SC-z}(x,y,-\frac{r_t}{2}) \end{cases} \tag{4}$$

where $B_{HC\text{-}x}$, $B_{HC\text{-}y}$, and $B_{HC\text{-}z}$ are the components of $\boldsymbol{B_{HC}}$ along the x-, y-, and z- axes, respectively.

The magnetic field of the TC is simulated and analyzed using the COMSOL Multiphysics software. Initially, a finite-element analytical model of the TC is established, as illustrated in Fig. 5(a). The TC is configured as a Helmholtz coil comprising a pair of identical circular coils with a diameter of 400 mm, a width of 60 mm, and 30 turns per coil. The center-to-center separation between the two coils is 200 mm, and the driving current applied to the TC is 6 A. The working region is defined as a cuboid region of 200 × 200 × 100 mm centered at the TC. Mesh refinement is applied to both the TC and the working region.

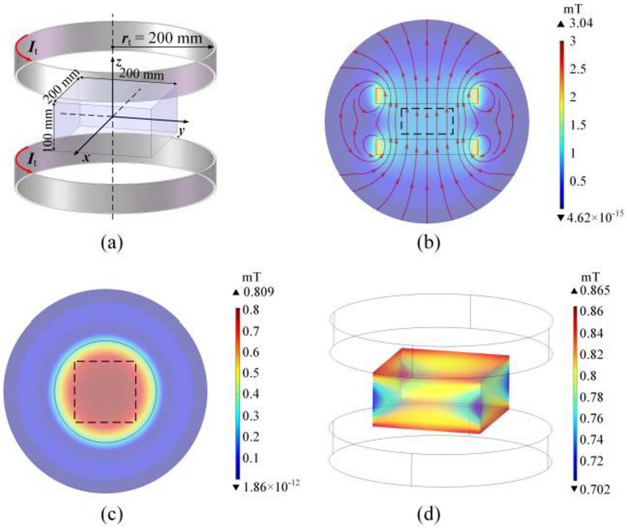

Fig. 5. Finite element analysis of the magnetic field of the TC. (a) Finite-element analytical model of the TC; magnetic field distribution (b) on the $x = 0/y = 0$ plane, (c) on the $z = 0$ plane, (d) in the working region.

The operating frequency selection involves critical trade-offs: excessively high frequencies increase susceptibility to external disturbances and risk detuning the receiving coil, while overly low frequencies lead to precipitous decline in transmission efficiency. According to the ICNIRP guidelines, under the same conditions, the electromagnetic safety is relatively higher within the frequency range of 1–100 kHz. Therefore, considering factors such as electromagnetic safety, system stability, and transmission efficiency, and combined with engineering practice, the operating frequency is set to 100 kHz.

The finite-element simulation results are presented in Fig. 5(b)–(d). Fig. 5(b) illustrates the magnetic flux density distribution on the $x = 0$ / $y = 0$ plane. It can be observed that the magnetic flux density is relatively uniform in the working region (indicated by the dashed line) and the magnetic field lines exhibit good perpendicularity. Fig. 5(c) displays the distribution of magnetic flux density on the $z = 0$ plane. It can be observed from the figure that the magnetic flux density is relatively more uniform in the working region. Fig. 5(d) presents the distribution of magnetic flux density in the working region, with a maximum value of 0.865 mT and a minimum value of 0.702 mT. It can be observed from the figure that the magnetic flux density is relatively higher at the corners of the working region (represented by the deep red), and it is comparatively lower at the middle of the vertical edges (deep blue).

B. Static Magnetic Field Analysis

The static magnetic field of a single rectangular permanent magnet is analyzed first. The dimensions of the rectangular permanent magnet are defined as $a \times b \times c$, and a Cartesian coordinate system is established, as shown in Fig. 6(a). The magnet is uniformly magnetized in the z-direction and reaches saturation.

According to the Ampere molecular circulation hypothesis, the magnetic field at any point in the external space of the magnet

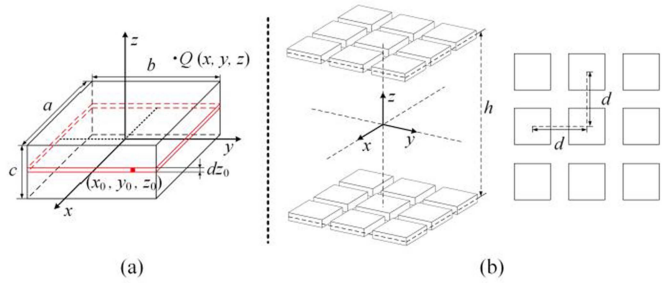

Fig. 6. Static magnetic field theoretical analysis of the (a) single rectangular permanent magnet, (b) EPM array.

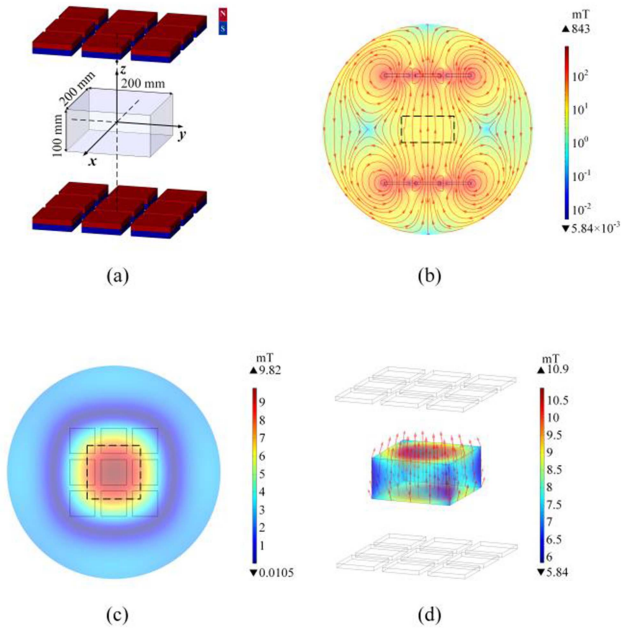

Fig. 7. Finite-element analysis of the magnetic field for the EPM array. (a) Finite-element analytical model of the EPM array; magnetic field distribution (b) on the $x = 0/y = 0$ plane, (c) on the $z = 0$ plane, (d) in the working region.

is generated by the closed current loop on the side surface of the permanent magnet. Let the coordinates of the magnetic field source be (x_0, y_0, z_0), and define the magnetization current density within the loop as J_s. A thin current loop with a thickness dz_0 is selected, having a current intensity of $J_s dz_0$. According to the relevant literature [29], the magnetic flux density $\boldsymbol{B_P}$ generated by the total current loop at any point $Q(x, y, z)$ outside the permanent magnet is expressed as (5) shown at the bottom of the next page.

The EPM array employs a double-layer structure with a distance h between the central cross sections of the two layers. Each layer consists of a 3×3 array of equally spaced rectangular permanent magnets, with a distance d between each magnet, as illustrated in Fig. 6(b). Each layer comprises a 3×3 array of rectangular permanent magnets equally spaced with a separation d, as illustrated in Fig. 6(b). Based on (5), the magnetic flux density $\boldsymbol{B_{PA}}$ of the static magnetic field of the EPM array is derived through coordinate transformation and is expressed in (6) shown at the bottom of the next page.

The magnetic field of the EPM array is simulated and analyzed using the COMSOL Multiphysics software. Initially, the finite element analytical model of the EPM array is established, as illustrated in Fig. 7(a). The permanent magnet material selected is a NdFeB magnet (N35), with dimensions $a = b = 95$ mm, $c = 10$ mm, $h = 400$ mm, and $d = 120$ mm. Mesh refinement is applied to both the working region ($200 \times 200 \times 100$ mm) and the EPM array. NdFeB is selected as the permanent magnet material due to its high remanence, making it suitable for miniaturization and lightweight applications. The design and optimization process of the EPM is detailed in the Appendix.

The finite-element analysis results are presented in Fig. 7(b)–(d). Fig. 7(b) presents the distribution of magnetic flux density on the $x = 0$ / $y = 0$ plane, indicating a good perpendicularity of the magnetic field lines in the working region. Fig. 7(c) shows the distribution of magnetic flux density on the $z = 0$ plane, revealing a relatively uniform distribution in the working region. Fig. 7(d) depicts the magnetic field distribution of the EPM array in the working region, with a maximum value of 10.9 mT and a minimum value of 5.84 mT. It can be observed from the figures that the value of the magnetic flux density decreases as the distance from the z-axis increases, while it increases as the distance from the $z = 0$ plane increases.

C. Coupled Magnetic Field Analysis

The mutual inductance M between the TC and the RC can be expressed as

$$M = \mu_r B_{HC} S_r \cos\alpha / I_t \tag{7}$$

where μ_r is the relative permeability of the medium, S_r is the total magnetic flux area of the RC, and α is the angle between the magnetic field vector $\boldsymbol{B_{HC}}$ and the normal to the plane of the RC. Assuming the static magnetic field $\boldsymbol{B_{PA}}$ generated by the EPM array is sufficiently strong to align the central axis of the RC with the direction of $\boldsymbol{B_{PA}}$. And the received power on the load P_L can be derived from (2) and (7), as shown in

$$\begin{cases} P_L = \dfrac{4\pi^2 f^2 {\mu_r}^2 {S_r}^2 R_L}{(R_r + R_L)^2} {B_e}^2 \\ B_e = \boldsymbol{B_{HC}} \cdot \dfrac{\boldsymbol{B_{PA}}}{|\boldsymbol{B_{PA}}|} \end{cases} \tag{8}$$

where B_e is defined as the effective magnetic flux density.

From (8), it can be observed that when the frequency of the driving voltage f and the design parameters of the receiving coil are fixed, the received power on the load P_L is positively linearly correlated with B_e^2. Based on the analysis of the alternating magnetic field and the static magnetic field, the effective magnetic flux density B_e in the working region can be determined. Due to its symmetry to the $x = 0$, $y = 0$, and $z = 0$ planes, data along the positive x, y, and z axes are selected to plot the distribution, as illustrated in Fig. 8. From Fig. 8, it can be observed that the maximum effective magnetic flux density $B_{e\text{-max}} = 0.8461$ mT is located at (100, 100, 50), and the minimum $B_{e\text{-min}} = 0.7009$ mT is situated at (100100,0). Fig. 9 presents contour plots of the effective magnetic flux density B_e on various planes ($z = 0$, 10, 20, 30, 40, 50 mm), providing a more intuitive representation of the distribution of B_e.

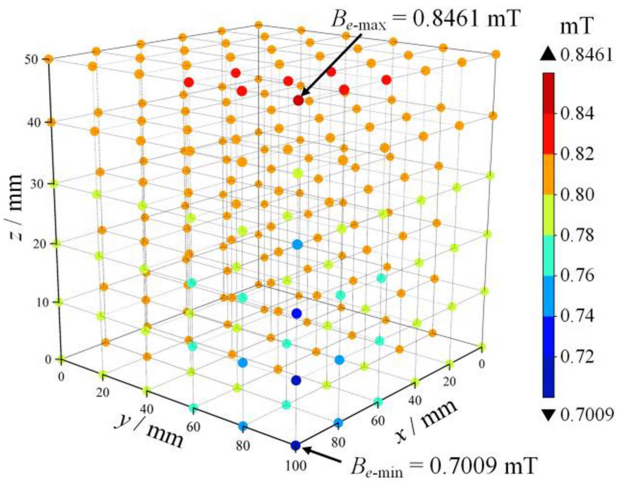

Fig. 8. Distribution of effective magnetic flux density B_e in the positive half-axis region.

TABLE I
ICNIRP REFERENCE THRESHOLD AND SIMULATION VALUES

	Whole-body average SAR (W /kg)	Local SAR (W/kg)	Internal electric field E(V/m)
ICNIRP	0.08	2	13.5
This article	1.08×10^{-6}	1.40×10^{-4}	1.02

D. Electromagnetic Safety Analysis

For medical instrumentation, electromagnetic safety analysis of the proposed system is critical. In accordance with ICNIRP guidelines [31], [32], restrictions apply to the SAR and internal electric field. This article employs Sim4Life software [33] for electromagnetic safety simulations. The simulations employ the female "Yoon-sun" anatomical human model. The coil model corresponds to the transmitting coil described in previous sections, configured with a driving current of 6 A and an operating frequency of 100 kHz.

The simulation results are presented in Fig. 10, with a comparison between ICNIRP guideline limits and corresponding simulated numerical values given in Table I. The whole-body average SAR of 1.08×10^{-6} W/kg and maximum local SAR of 1.40×10^{-4} W/kg, along with an internal electric field of $E =$ 1.02 V/m, are all significantly lower than the ICNIRP safety thresholds, thereby demonstrating the electromagnetic safety compliance of the proposed system.

$$
\begin{cases}
\boldsymbol{B_P} = B_{P-x}\boldsymbol{i} + B_{P-y}\boldsymbol{j} + B_{P-z}\boldsymbol{k} \\
B_{P-x} = \frac{\mu_0 J_s}{8\pi}\left[-\Gamma(-x+\frac{a}{2}, -y+\frac{b}{2}, z+\frac{c}{2}) - \Gamma(-x+\frac{a}{2}, y+\frac{b}{2}, z+\frac{c}{2}) + \Gamma(x+\frac{a}{2}, -y+\frac{b}{2}, z+\frac{c}{2})\right. \\
\qquad \left. + \Gamma(x+\frac{a}{2}, y+\frac{b}{2}, z+\frac{c}{2})\right] \\
B_{P-y} = \frac{\mu_0 J_s}{8\pi}\left[-\Gamma(-y+\frac{b}{2}, -x+\frac{a}{2}, z+\frac{c}{2}) - \Gamma(-y+\frac{b}{2}, x+\frac{a}{2}, z+\frac{c}{2}) + \Gamma(y+\frac{b}{2}, -x+\frac{a}{2}, z+\frac{c}{2})\right. \\
\qquad \left. + \Gamma(x+\frac{a}{2}, y+\frac{b}{2}, z+\frac{c}{2})\right] \\
B_{P-z} = -\frac{\mu_0 J_s}{4\pi}\left[\Phi(-y+\frac{b}{2}, -x+\frac{a}{2}, z+\frac{c}{2}) + \Phi(y+\frac{b}{2}, -x+\frac{a}{2}, z+\frac{c}{2}) + \Phi(-x+\frac{a}{2}, -y+\frac{b}{2}, z+\frac{c}{2})\right. \\
\qquad + \Phi(x+\frac{a}{2}, -y+\frac{b}{2}, z+\frac{c}{2}) \\
\left. + \Phi(-y+\frac{b}{2}, x+\frac{a}{2}, z+\frac{c}{2}) + \Phi(y+\frac{b}{2}, x+\frac{a}{2}, z+\frac{c}{2}) + \Phi(-x+\frac{a}{2}, y+\frac{b}{2}, z+\frac{c}{2}) + \Phi(x+\frac{a}{2}, y+\frac{b}{2}, z+\frac{c}{2})\right] \\
\Gamma(\varphi_1, \varphi_2, \varphi_3) = \ln \left.\frac{\sqrt{\varphi_1^2+\varphi_2^2+(\varphi_3-z_0)^2}-\varphi_2}{\sqrt{\varphi_1^2+\varphi_2^2+(\varphi_3-z_0)^2}+\varphi_2}\right|_{z_0=-\frac{c}{2}}^{z_0=\frac{c}{2}} \\
\Phi(\phi_1, \phi_2, \phi_3) = \begin{cases} \left.\arctan\left[\frac{\phi_1}{\phi_2}\frac{\phi_3-z_0}{\sqrt{\phi_1^2+\phi_2^2+(\phi_3-z_0)^2}}\right]\right|_{z_0=-\frac{c}{2}}^{z_0=\frac{c}{2}} & (y \neq 0) \\ 0 \; (y=0) \end{cases}
\end{cases}
\tag{5}
$$

$$
\begin{aligned}
\boldsymbol{B_{PA}} = {} & \boldsymbol{B_P}\left(x-d, y, -\frac{h}{2}\right) + \boldsymbol{B_P}\left(x-d, y, \frac{h}{2}\right) + \boldsymbol{B_P}\left(x+d, y, -\frac{h}{2}\right) + \boldsymbol{B_P}\left(x+d, y, \frac{h}{2}\right) + \boldsymbol{B_P}\left(x, y-d, -\frac{h}{2}\right) \\
& + \boldsymbol{B_P}\left(x, y-d, \frac{h}{2}\right) \\
& + \boldsymbol{B_P}\left(x, y+d, -\frac{h}{2}\right) + \boldsymbol{B_P}\left(x, y+d, \frac{h}{2}\right) + \boldsymbol{B_P}\left(x-d, y-d, -\frac{h}{2}\right) + \boldsymbol{B_P}\left(x-d, y-d, \frac{h}{2}\right) \\
& + \boldsymbol{B_P}\left(x-d, y+d, -\frac{h}{2}\right) + \boldsymbol{B_P}\left(x-d, y+d, \frac{h}{2}\right) \\
& + \boldsymbol{B_P}\left(x+d, y-d, -\frac{h}{2}\right) + \boldsymbol{B_P}\left(x+d, y-d, \frac{h}{2}\right) + \boldsymbol{B_P}\left(x+d, y+d, -\frac{h}{2}\right) + \boldsymbol{B_P}\left(x+d, y+d, \frac{h}{2}\right) \\
& + \boldsymbol{B_P}\left(x, y, -\frac{h}{2}\right) + \boldsymbol{B_P}\left(x, y, \frac{h}{2}\right).
\end{aligned}
\tag{6}
$$

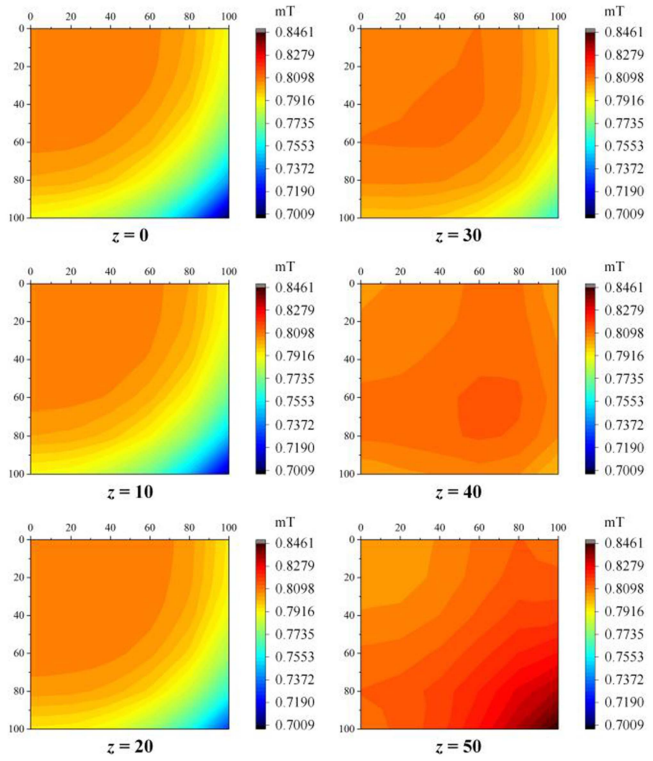

Fig. 9. Contour plots of the effective magnetic flux density B_e on various planes.

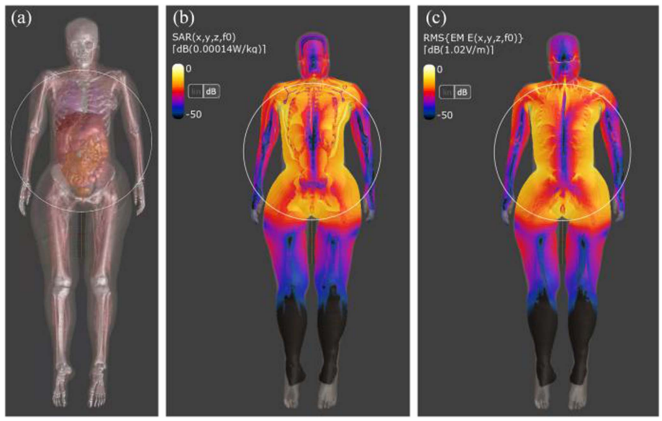

Fig. 10. Electromagnetic safety finite element analysis. (a) "Yoon-sun" anatomical human model. (b) Simulation results of the SAR distribution. (c) Simulation results of the internal electric field E distribution.

IV. Prototype and Experiment

A. Prototype of the SOWPT System

Fig. 11 illustrates the external module prototype of the SOWPT system, including the TC, EPM array, and circuit components. The TC is a Helmholtz coil wound with ϕ0.1 mm × 300 strands of Litz wire, comprising a total of 60 turns. The relevant parameters are presented in Table II.

The internal module prototype of the SOWPT system is illustrated in Fig. 12, comprising the gyroscope-inspired PRD and the

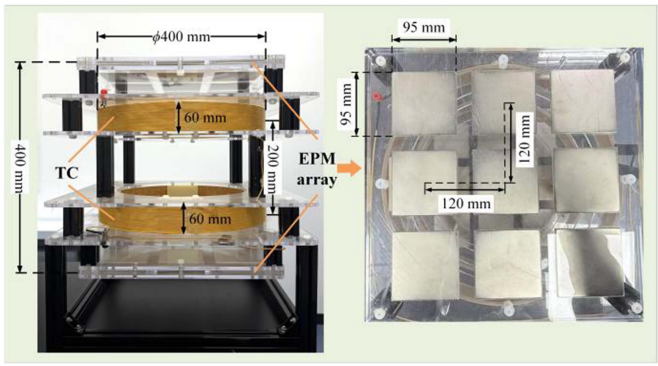

Fig. 11. External module prototype of the SOWPT system.

TABLE II
Relevant Parameters of the TC and RC

Coil	Wire specification	Medium	C_s/nF	R_s/Ω	L_s/uH	Q
TC	ϕ0.1×300 60 turns	without EPM	-1.74	1.64	1457.6	558.44
		with EPM	-1.79	4.29	1416.7	207.50
RC	ϕ0.12 208 turns	without IPM	-9.95	8.20	254.69	19.52
		with IPM	-10.82	32.88	234.19	4.48

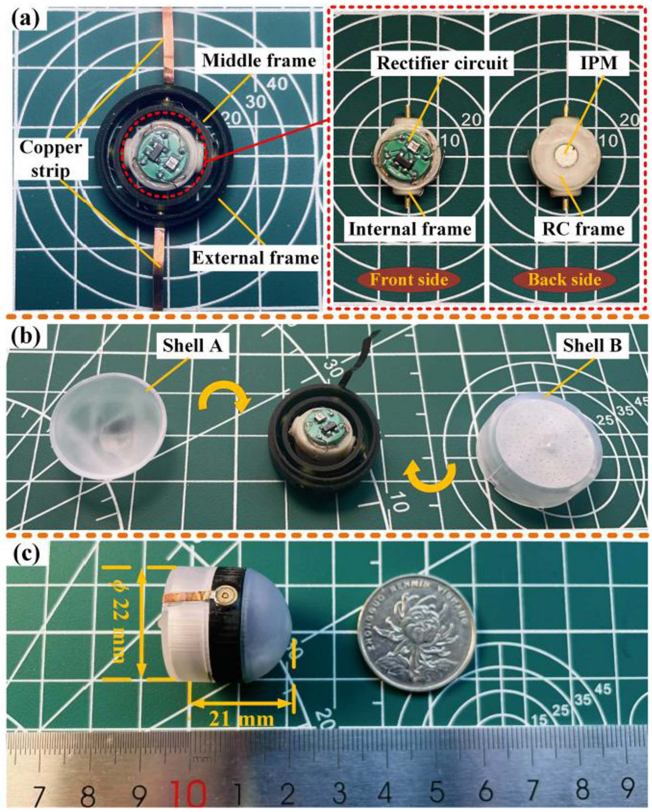

Fig. 12. Internal module prototype of the SOWPT system. (a) Structure of the PRD. (b) Assembly process of the PRD. (c) Overall view of the PRD.

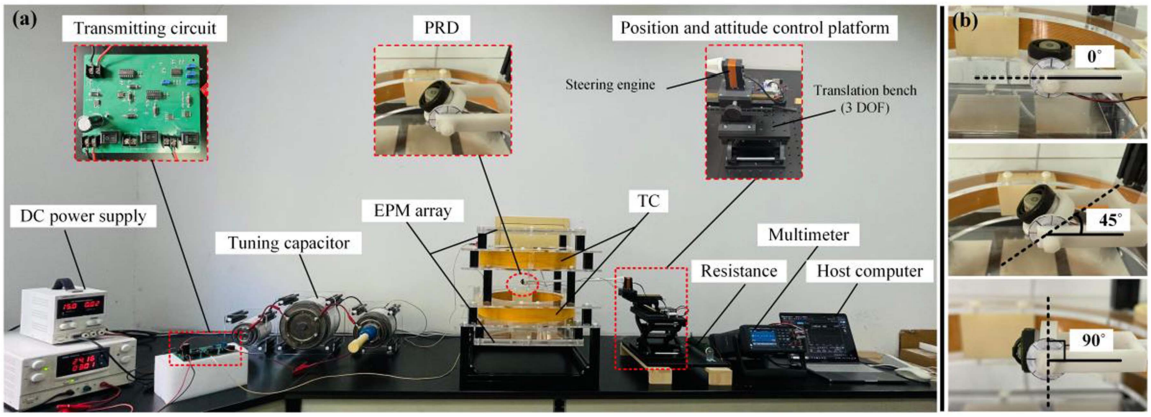

Fig. 13. (a) Experimental testbed for the SOWPT system. (b) Three attitude angles of the PRD for testing: 0°, 45°, and 90°.

receiving circuit. The various frames and shells of the PRD are fabricated using photosensitive resin via 3-D printing owing to its simplified manufacturing process. The RC frame and internal frame utilize the photosensitive resin RSN-201, characterized by higher hardness, while the middle frame and external frame employ the photosensitive resin RSN-501, offering greater toughness. Shell A and shell B are constructed from the photosensitive resin RSN-709. Fig. 12(a) shows the internal structure of the PRD. The material of the IPM is NdFeB magnets (N52) with dimensions of $\phi 4 \times 6$ mm. The IPM is installed at the center of the RC frame. The RC is wound around the RC frame using $\phi 0.12$ mm enameled wire, with a total of 208 turns. The relevant parameters of the RC are given in Table II. The rectifier circuit converts the alternating current generated by the RC into direct current, utilizing the BAS4002A rectifier chip. The copper bar is connected to the outermost bearing base, serving as a conductor to transmit the generated power to the load. Fig. 12(b) depicts the assembly process. Fig. 12(c) shows the overall view of the PRD, with dimensions of $\phi 22 \times 21$ mm and a total weight of 5.43 g.

B. Received Power Experiment

To evaluate the performance of the SOWPT system prototype, an experimental testbed is constructed, as shown in Fig. 13(a). This experimental testbed consists of an external module, an internal module, and a data acquisition module. The external module comprises a DC power supply, a transmitting circuit, a tuning capacitor, an EPM array, and a TC. The internal module includes a PRD and a receiving circuit. The data acquisition module consists of a position and attitude control platform, an equivalent resistance, a multimeter, and a host computer. The position and control platform can drive the PRD to rotate at a predetermined speed, simulating the actual motion of the MCR in the gastrointestinal tract. Based on prior research [30], the equivalent resistance is set to 30 Ω to simulate the operational load of the MCR. A multimeter is used to measure the voltage across the equivalent resistance in real-time, thereby determining the received power on the load. The frequency f of the alternating current applied to the TC is set to 100 kHz.

Two metrics are employed to evaluate the robustness of the SOWPT system: the normalized standard deviation (NSD) and maximum-to-minimum ratio (MMR) of the received power on the load, defined in (9). Lower NSD and MMR values indicate enhanced system robustness and more stable power transfer

$$\begin{cases} \sigma_{PL} = \sqrt{\dfrac{\sum_{i=1}^{n}\left(P_{Li}-\overline{P_L}\right)^2}{n\overline{P_L}^2}} \\ \lambda_{PL} = \dfrac{\max(P_{Li})}{\min(P_{Li})} \end{cases} \tag{9}$$

where P_{Li} are the measurement values of the received power on the load, $\sigma_{PL}$is the NSD of the P_{Li}, and $\lambda_{PL}$is the MMR of the P_{Li}.

Fig. 14 illustrates the variation of the received power on the load over time at six representative positions, with the PRD oriented at angles of 0°, 45°, and 90° [see Fig. 13(b)] relative to the horizontal direction, while rotating at a speed of 20 r/min. The data has been fitted with a second-order polynomial to reflect the trend of the variation. From the figure, it can be observed that at the angle of 0° (represented by the red line), the average received power on the load is higher than that at 45° (blue line) and 90° (green line). Additionally, the NSD is generally lower at 0° compared to the other two angles, indicating that the device exhibits superior robustness when positioned at 0°. When the PRD is positioned at the vertical edge of the working region, specifically at (100, 100, 0) and (100, 100, 50), the received power on the load exhibits significant fluctuations. At the position (100, 100, 0) with an angle of 90°, the NSD and MMR reach the maximum values of 13.86% and 163.41%, respectively. NSD and MMR values of P_L measurement data are given in Table III.

Fig. 15 presents a comparison between the average experimental values of P_L and the theoretical values of B_e^2 at various positions. According to (8), under fixed design parameters, P_L is positively linearly correlated with B_e^2. The figure demonstrates that the trend of the experimental values of P_L is consistent with that of the theoretical values of B_e^2, aligning with the theoretical analysis and thereby validating the correctness of the theoretical model.

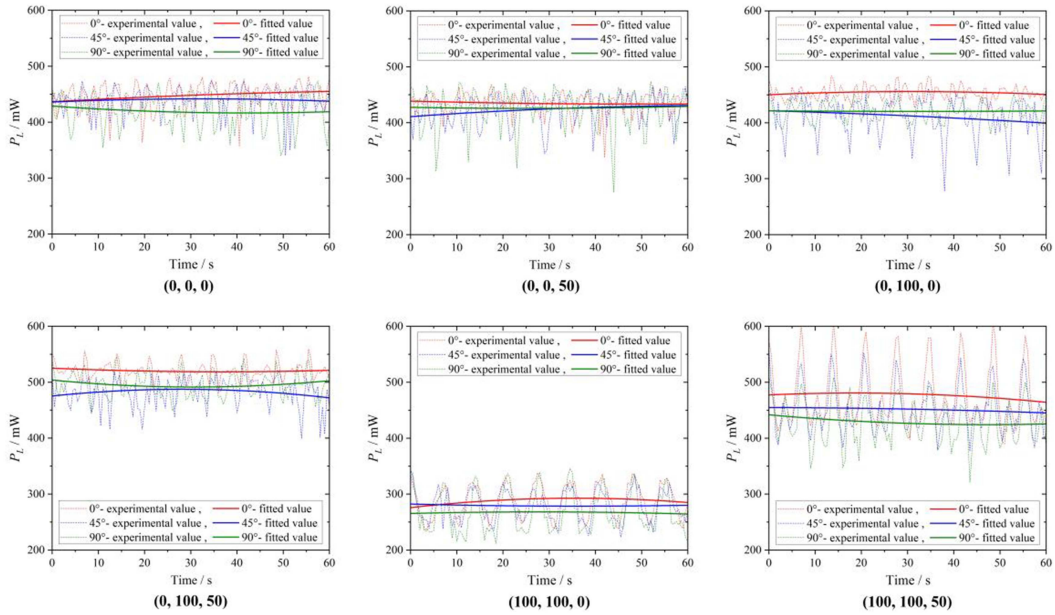

Fig. 14. Experimental values of P_L with three attitude angles at various positions.

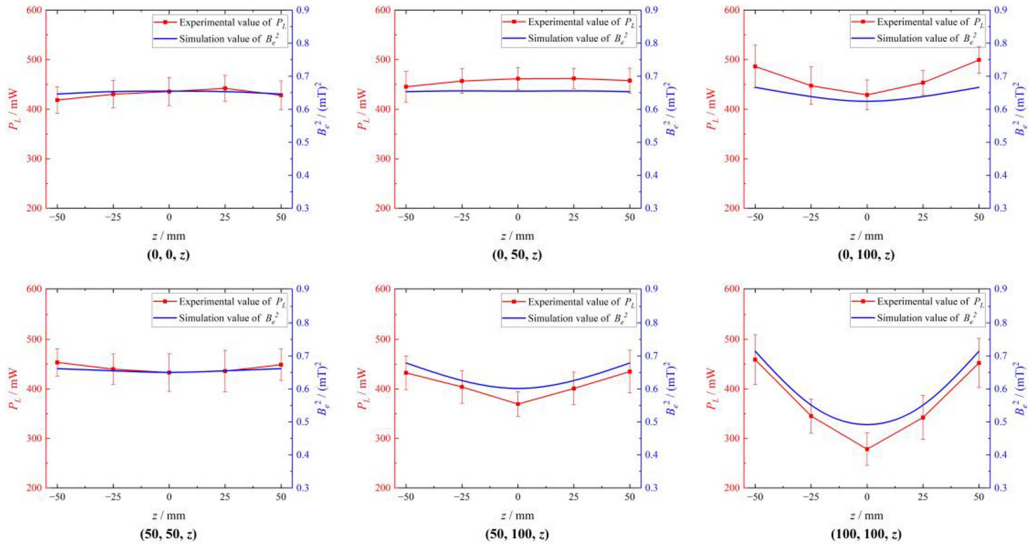

Fig. 15. Comparison between the average experimental values of P_L and the theoretical values of Be^2 at various positions.

C. Temperature Rise Test

The RC induces a temperature rise of the PRD during operation due to Joule heating effects. For ingestible capsule robots, such thermal variations represent a critical safety consideration. Therefore, temperature rise of the PRD during operation is conducted using infrared thermography, as shown in Fig. 16. The test is conducted under an ambient temperature of 24.2 ± 1 °C, with the PRD temperature recorded at 5-min intervals over a duration of 60 min. The test results are shown in Fig. 17. As observed from the figure, the maximum temperature rise of the PRD is $\Delta T_{\max} = 3.6$ °C. The human gastrointestinal tract temperature typically ranges from 37.0 °C to 38.5 °C. Furthermore, during MCR procedures, patients are required to ingest fluid for intestinal lumen expansion, which further reduces the actual

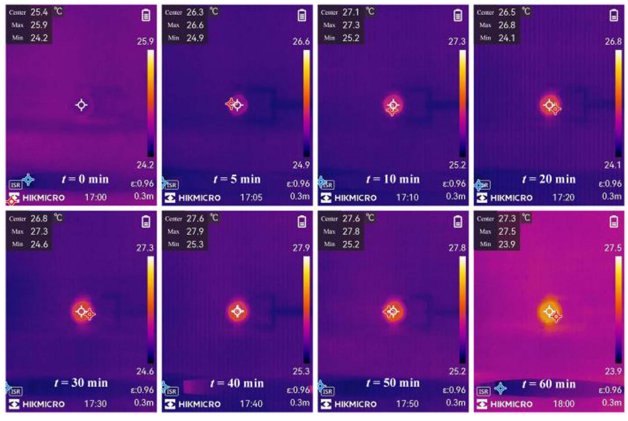

Fig. 16. Thermal characterization experiment of the PRD.

TABLE III
NSD AND MMR VALUES OF P_L MEASUREMENT DATA

Position	Attitude	NSD/%	MMR/%
(0, 0, 0)	0°	5.37	134.79
	45°	5.46	139.08
	90°	7.13	139.37
(0, 0, 50)	0°	4.61	135.29
	45°	6.32	138.64
	90°	8.51	171.72
(0, 100, 0)	0°	2.91	114.92
	45°	8.66	166.49
	90°	4.06	118.97
(0, 100, 50)	0°	2.97	116.35
	45°	5.54	132.77
	90°	4.45	122.70
(100, 100, 0)	0°	10.10	144.24
	45°	9.84	154.25
	90°	13.86	163.41
(100, 100, 50)	0°	11.55	155.98
	45°	9.14	148.05
	90°	9.31	158.95

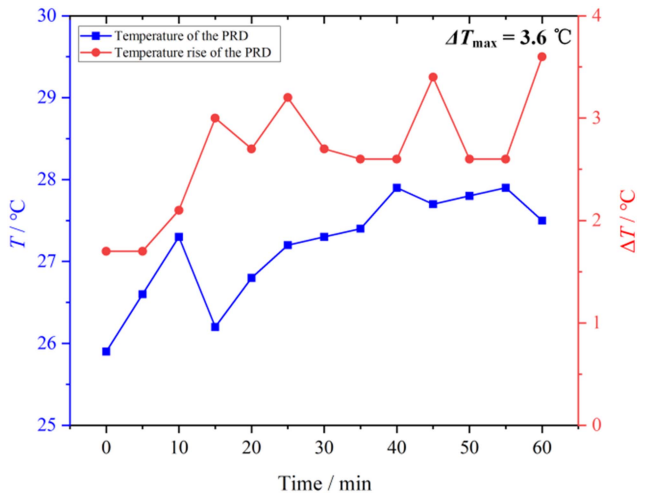

Fig. 17. Time-dependent curves of the PRD temperature and temperature rise.

temperature rise of the PRD below $\Delta T_{\max}$. According to the international standard IEC 60601-1, the contact temperature for ingestible medical devices must remain below 43 °C. Therefore, the temperature rise of the PRD developed in this article remains within the safe operating range.

V. DISCUSSION

The experimental results indicate that at the 0° orientation, the received power on the load exhibits a higher average value and a lower fluctuation amplitude compared to the 45° and 90° orientations. This is attributed to higher resistance at the 45° and 90° orientations caused by machining and assembly errors. Furthermore, the results show that the P_L fluctuation amplitude increases with distance from the z-axis. Combined with the static magnetic field simulation analysis of the EPM array, it can be inferred that the farther the distance from the z-axis, the weaker the magnetic field intensity of the EPM array. This results in a smaller magnetic force maintaining the coil orientation, thus leading to increased fluctuations in the received power on the load.

The 1DTC-3DRC configuration offers advantages in terms of relative simplicity at the transmitter side, but suffers from significant power fluctuations and poor stability. The 3DTC-1DRC configuration benefits from a relatively simple receiver design, saving space for the MCR; however, it is plagued by strong mutual inductance among the three individual TC, making it difficult to control the direction of the resultant magnetic field and leading to large power variations. The rotating 1DTC-1DRC topology achieves higher power transfer efficiency, yet requires complex structures at both transmitter and receiver ends, exhibits poor real-time response, and struggles to provide a stable power supply. The SOWPT system developed in this article demonstrates the capability of real-time self-alignment to maintain one-dimensional coupling, and the power supply stability has been verified through correlation analysis and experiments. The current prototype still has a relatively large size, which will be optimized in future work.

Therefore, future work will focus on optimizing the system in the following aspects.

1) Enhancing the machining and assembly precision of the PRD to reduce resistance during the rotation of the gyroscope-inspired mechanism.
2) Optimizing the EPM array to address the issue of increased fluctuations in the received power at the edges of the working region.
3) Optimizing the structure of the PRD to reduce its size without compromising the received power.

VI. CONCLUSION

This article proposes an SOWPT system designed for powering the MCR. This system enables stable wireless power transfer for the MCR with omnidirectional attitude through the design of a novel gyroscope-inspired PRD. An experimental testbed is established to test the developed SOWPT system prototype. Experimental results demonstrate that, compared to conventional WPT systems for the MCR, the proposed system exhibits reduced received power fluctuation and enhanced robustness, thereby significantly improving the stability and reliability of the MCR. Furthermore, the experimental results validate the accuracy of the proposed magnetic field theoretical model, which provides a theoretical foundation for further optimization of the SOWPT system.

APPENDIX

The design and optimization process of the EPM is as follows. Simulation results indicate that the maximum angle between the magnetic force vector and the vertical direction within the working region occurs at the eight vertices, for instance, at coordinates (100, 100, 50). The z-axis magnetic flux density

TABLE IV
OPTIMIZATION DATA FOR A SINGLE BULK PERMANENT MAGNET

Side length / mm	$B_{PA\text{-}x}$ / mT	$B_{PA\text{-}y}$ / mT	$B_{PA\text{-}z}$ / mT	β / deg
300	-3.5459	-3.5445	9.2199	28.54
350	-3.1279	-3.1262	10.8450	22.18
360	-3.0064	-3.0051	11.0290	21.08
370	-2.8701	-2.8731	11.1600	20.00
380	-2.7278	-2.7296	11.2390	18.95
390	-2.5824	-2.5817	11.2600	17.97
400	-2.4352	-2.4348	11.2230	17.06

TABLE V
OPTIMIZATION DATA FOR 3 × 3 EPM ARRAY

d / mm	$B_{PA\text{-}x}$ / mT	$B_{PA\text{-}y}$ / mT	$B_{PA\text{-}z}$ / mT	β / deg
100	-3.2266	-3.2315	8.4164	28.48
110	-2.5263	-2.5235	7.9736	24.12
120	**-1.8646**	**-1.8649**	**7.2877**	**19.89**
130	-1.2838	-1.2849	6.3966	15.85

$B_{PA\text{-}z}$ (100, 100, 50) is maximized under the design constraints that the angle β between the magnetic field direction and vertical axis at these locations does not exceed 20°, and the side length l_{PA} of the EPM remains within 400 mm (diameter of the TC), as specified in

$$\begin{cases} \beta \leq 20^\circ \\ l_{PA} \leq 400 \text{ mm} \\ \max B_{PA-z}\,(100, 100, 50) \end{cases}. \tag{10}$$

Simulation analysis revealed that employing a single bulk permanent magnet as the EPM would require dimensions exceeding 370 × 370 mm to satisfy the design specifications, as given in Table IV. However, such a monolithic magnet configuration would generate significant eddy current losses, necessitate custom manufacturing, and incur high cost. Consequently, an EPM array is constructed using commercially available 95 × 95 × 10 mm NdFeB magnets (N35). Through finite element analysis, a 3 × 3 array configuration is implemented. The distance d is systematically optimized by adjusting it in 10 mm increments through iterative simulations, with the results given in Table V. Based on the design requirements, $d = 120$ mm is determined to be the optimal configuration.

ACKNOWLEDGMENT

The authors would like to thank ZMT Zurich MedTech AG for providing Sim4Life software.

REFERENCES

[1] F. Bray et al., "Global cancer statistics 2022: GLOBOCAN estimates of incidence and mortality worldwide for 36 cancers in 185 countries," *Ca-A Cancer J. Clinicians*, vol. 74, no. 3, pp. 229–263, May 2024.
[2] G. Iddan, G. Meron, A. Glukhovsky, and P. Swain, "Wireless capsule endoscopy," *Nature*, vol. 405, no. 6785, May 2000, Art. no. 417.
[3] W. Wang, G. Z. Yan, D. Han, Y. C. Meng, and P. X. Pu, "Design and testing of a novel gastrointestinal microrobot," *Biomed. Microdevices*, vol. 22, no. 1, Nov. 2020, Art. no. 82.
[4] N. Ebrahimi et al., "Magnetic actuation methods in bio/soft robotics," *Adv. Funct. Mater.*, vol. 31, no. 11, Mar. 2021, Art. no. 2005137.
[5] S. Kim, S. Bae, W. Lee, and G. Jang, "Magnetic navigation system composed of dual permanent magnets for accurate position and posture control of a capsule endoscope," *IEEE Trans. Ind. Electron.*, vol. 71, no. 1, pp. 739–748, Jan. 2024.
[6] H. S. Lee, Y. Ko, and C. S. Kim, "Enhanced motion control of magnetically actuated capsule robot using mema-a mobile electromagnetic actuation system," *IEEE/ASME Trans. Mechatron.*, vol. 30, no. 2, pp. 933–944, Apr. 2025.
[7] J. Y. Gao, Z. L. Zhang, and G. Z. Yan, "Locomotion analysis of a clamper-based capsule robot in a compliant tube," *IEEE/ASME Trans. Mechatron.*, vol. 26, no. 1, pp. 55–65, Feb. 2021.
[8] C. Zhou et al., "An ingestible near-infrared fluorescence capsule endoscopy for specific gastrointestinal diagnoses," *Biosensors Bioelectron.*, vol. 257, Aug. 2024, Art. no. 116209.
[9] W. Wang, C. Zhou, J. L. Jiang, X. Y. Cui, G. Z. Yan, and D. X. Cui, "Optimization of wireless power receiving coil for near-infrared capsule robot," *J. Shanghai Jiaotong Univ. (Sci.)*, vol. 30, no. 3, pp. 425–432, Jun. 2025.
[10] N. J. Greenidge et al., "Harnessing the oloid shape in magnetically driven robots to enable high-resolution ultrasound imaging," *Sci. Robot.*, vol. 10, no. 100, Mar. 2025, Art. no. eadq4198.
[11] S. Song et al., "Integrated design and decoupled control of anchoring and drug release for wireless capsule robots," *IEEE/ASME Trans. Mechatron.*, vol. 27, no. 5, pp. 2897–2907, Oct. 2022.
[12] D. X. Ye et al., "Design and control of a magnetically-actuated capsule robot with biopsy function," *IEEE Trans. Biomed. Eng.*, vol. 69, no. 9, pp. 2905–2915, Sep. 2022.
[13] P. Shokrollahi et al., "Blindly controlled magnetically actuated capsule for noninvasive sampling of the gastrointestinal microbiome," *IEEE/ASME Trans. Mechatron.*, vol. 26, no.no. 5, pp. 2616–2628, Oct. 2021.
[14] Y. X. Sun et al., "Magnetically driven capsules with multimodal response and multifunctionality for biomedical applications," *Nature Commun.*, vol. 15, no.no. 1, Feb. 2024, Art. no. 1839.
[15] S. S. Srinivasan et al., "A vibrating ingestible bioelectronic stimulator modulates gastric stretch receptors for illusory satiety," *Sci. Adv.*, vol. 9, no. 51, Dec. 2023, Art. no. eadj3003.
[16] G. Arrick et al., "Cephalopod-inspired jetting devices for gastrointestinal drug delivery," *Nature*, vol. 636, no. 8042, pp. 481–487, Dec. 2024.
[17] Q. Ke, W. J. Luo, G. Z. Yan, and K. Yang, "Analytical model and optimized design of power transmitting coil for inductively coupled endoscope robot," *IEEE Trans. Biomed. Eng.*, vol. 63, no. 4, pp. 694–706, Apr. 2016.
[18] H. Y. Zhuang, W. Wang, and G. Z. Yan, "Ferrite concentrating and shielding structure design of wireless power transmitting coil for inductively coupled capsule robot," *IEEE Trans. Biomed. Circuits Syst.*, vol. 17, no.no. 1, pp. 45–53, Feb. 2023.
[19] W. Wang et al., "A novel expanding mechanism of gastrointestinal microrobot: Design, analysis and optimization," *Micromachines*, vol. 10, no. 11, Nov. 2019, Art. no. 724.
[20] M. R. Basar, M. Y. Ahmad, J. Cho, and F. Ibrahim, "An improved wearable resonant wireless power transfer system for biomedical capsule endoscope," *IEEE Trans. Ind. Electron.*, vol. 65, no. 10, pp. 7772–7781, Oct. 2018.
[21] J. Y. Gao et al., "Design and optimization of a novel double-layer Helmholz coil for wirelessly powering a capsule robot," *IEEE Trans. Power Electron.*, vol. 39, no. 1, pp. 1826–1839, Jan. 2024.
[22] Y. C. Meng et al., "A novel wireless power transfer system with two parallel opposed coils for gastrointestinal capsule robot," *Sensors Actuators A, Phys.*, vol. 321, Apr. 2021, Art. no. 112413.
[23] Z. W. Jia, G. Z. Yan, H. Liu, Z. W. Wang, P. P. Jiang, and Y. Shi, "The optimization of wireless power transmission: Design and realization," *Int. J. Med. Robot. Comput. Assist. Surg.*, vol. 8, no. 3, pp. 337–347, Sep. 2012.
[24] H. Zhang, Z. Li, and C. K. Lee, "Transmitter adaptation and wireless power control for capsule endoscopy," *IEEE Trans. Power Electron.*, vol. 39, no. 4, pp. 4884–4894, Apr. 2024.

[25] R. Q. Wen, G. Z. Yan, S. Kuang, D. Han, P. P. Jiang, and Z. W. Wang, "Novel three-dimensional combined transmitting coils applied for gastrointestinal capsule robot," *Sensors Actuators A, Phys.*, vol. 383, Mar. 2025, Art. no. 116188.
[26] D. Han et al., "Stable wireless power transfer system for capsule robot using three-dimensional hybrid transmitting coil pairs," *IEEE Trans. Power Electron.*, vol. 40, no. 6, pp. 8824–8833, Jun. 2025.
[27] J. Y. Gao et al., "Stable wireless power transmission for a capsule robot with randomly changing attitude," *IEEE Trans. Power Electron.*, vol. 38, no. 2, pp. 2782–2796, Feb. 2023.
[28] H. Y. Zhuang, W. Wang, and G. Z. Yan, "Omnidirectional wireless power transfer system using modified saddle-shaped coil pair for implantable capsule robots," *IEEE Trans. Power Electron.*, vol. 38, no. 9, pp. 11664–11672, Sep. 2023.
[29] X. F. Gou, Y. Yang, and X. J. Zheng, "Analytic expression of magnetic field distribution of rectangular permanent magnets," *Appl. Math. Mech. (English Ed.)*, vol. 25, no. 3, pp. 298–306, Mar. 2004.
[30] R. Q. Wen et al., "Two-dimensional ferrite core-based transmitting coil for wireless power transfer in novel capsule robots," *J. Power Electron.*, vol. 24, no. 12, pp. 1956–1965, Dec. 2024.
[31] International Commission on Non-Ionizing Radiation Protection, "Guidelines for limiting exposure to electromagnetic fields (100 kHz to 300 GHz)," *Health Phys.*, vol. 118, no. 5, pp. 483–524, May 2020.
[32] International Commission on Non-Ionizing Radiation Protection, "Guidelines for limiting exposure to time-varying electric and magnetic fields (1 Hz to 100 kHz)," *Health Phys.*, vol. 99, no. 6, pp. 818–836, Dec. 2010.
[33] Sim4Life. [Online]. Available: https://www.sim4life.swiss

Wei Wang received the B.S. and M.S. degrees in mechanical engineering from Wuhan University of Technology, Wuhan, China, in 2012 and 2015, respectively, and the Ph.D. degree in instrument science and technology from Shanghai Jiao Tong University, Shanghai, China, in 2020.

He is currently a Postdoctoral Researcher with the School of Automation and Intelligent Sensing, Shanghai Jiao Tong University, Shanghai, China. His research interests include intelligent medical systems, medical precision instruments, and gastrointestinal microrobots.

Jinlei Jiang was born in Zhejiang, China, in 1999. He received the B.E. degree in mechanical engineering from Shanghai Jiao Tong University, Shanghai, China, in 2022, where he is currently working toward the Ph.D. degree in instrument science and technology with the School of Automation and Intelligent Sensing.

His research interests include magnetic navigation, wireless power transmission, and the design of ingestible capsule robots for specific gastric diseases.

Weicheng Wang was born in Hebei, China, in 1997. He received the M.S. degree in electrical engineering from Northeast Petroleum University, Daqing, China, in 2023, where he is currently working toward the Ph.D. degree in electronic information with the School of Automation and Intelligent Sensing.

His research interests include the development of multimodal imaging techniques for capsule endoscopy for the diagnosis of early gastrointestinal cancers.

Xinyuan Cui received the M.M. degree in medical imaging and nuclear medicine from Shanghai Jiao Tong University School of Medicine, Shanghai, China, in 2025, where he is currently working toward the Ph.D. degree in medical technology with the School of Medicine.

His research primarily focuses on the integration of medical imaging technology and nanomedicine.

Guozheng Yan was born in Hunan, China, in 1961. He received the Ph.D. degree in mechanical engineering rom Jilin University of Technology, Jilin, China, in 1993.

In 1995, he became a Postdoctoral Fellow with the Nanjing University of Aeronautics and Astronautics, Nanjing, China. In 1997, he was a Professor with Shanghai Jiao Tong University, Shanghai, China. His research interests include biomedical electronics, microsensors, microelectromechanical systems, and instrument engineering.

Daxiang Cui was born in Anhui, China, in 1967. He received the B.M. degree in clinical medicine from Naval Medical University, Shanghai, China, in 1990, and the M.M. and the Ph.D. degrees in biochemistry and molecular biology from Air Force Medical University, Xi'an, China, in 1995 and 1998, respectively.

He is currently the Chair Professor with Shanghai Jiao Tong University, the Vice Dean of the Translational Medicine Research Institute, and the Head of the Nano-Biotechnology Research Institute. He was selected as a "Highly Cited Chinese Researchers" in 2022. His research interests include nanomaterials synthesis and safety evaluation, multifunctional Nano-Probes and molecular imaging, and efficient gene or drug delivery systems.